Multiple-coil k-space interpolation enhances resolution in single-shot spatiotemporal MRI

FULL PAPER

Magnetic Resonance in Medicine 00:00–00 (2017)

Multiple-Coil *k*-Space Interpolation Enhances Resolution in Single-Shot Spatiotemporal MRI

Gilad Liberman,[1] Eddy Solomon,[1] Michael Lustig,[2] and Lucio Frydman[1]*

Purpose: Spatio-temporal encoding (SPEN) experiments can deliver single-scan MR images without folding complications and with robustness to chemical shift and susceptibility artifacts. Further resolution improvements are shown to arise by relying on multiple receivers, to interpolate the sampled data along the low-bandwidth dimension. The ensuing multiple-sensor interpolation is akin to recently introduced SPEN interleaving procedures, albeit without requiring multiple shots.

Methods: By casting SPEN's spatial rasterization in *k*-space, it becomes evident that local *k*-data interpolations enabled by multiple receivers are akin to real-space interleaving of SPEN images. The practical implementation of such a resolution-enhancing procedure becomes similar to those normally used in simultaneous acquisition of spatial harmonics or sensitivity encoding, yet relaxing these methods' fold-over constraints.

Results: Experiments validating the theoretical expectations were carried out on phantoms and human volunteers on a 3T scanner. The experiments showed the expected resolution enhancement, at no cost to the sequence's complexity. With the addition of multibanding and stimulated echo procedures, 48-slice full-brain coverage could be recorded free from distortions at submillimeter resolution, in 3 s.

Conclusions: Super-resolved SPEN with SENSE (SUSPENSE) achieves the goals of multishot SPEN interleaving delivering single-shot submillimeter in-plane resolutions in scanners equipped with suitable multiple sensors. **Magn Reson Med 000:000–000, 2017. © 2017 International Society for Magnetic Resonance in Medicine.**

Key words: SPEN; parallel imaging; resolution enhancement; single-scan MRI

INTRODUCTION

Spatiotemporal encoding (SPEN) presents an alternative to usual time-domain or *k*-space approaches, which can deliver multidimensional magnetic resonance (NMR) spectra or images (MRI) in a single scan (1–11). Spatiotemporal encoding relies on a linear excitation or inversion of the spins as a function of time. This imposes linear and quadratic evolution phases on the spin-packets throughout the field of view (FOV) (12–14); the linear dephasing is the basis of single-scan 2D NMR spectroscopy (5,15–17), whereas the quadratic one opens an alternative route to single-scan 2D MRI (1–11). Spatiotemporal encoding differs from either conventional 2D NMR or MRI by the fact that the spectral or spatial information that it delivers arises as direct observable in the time/*k*-domain; i.e., without a need for Fourier transforming the acquired data. In the imaging case this can be understood by considering the consequences of applying a chirped inversion pulse of duration T_e and bandwidth BW, while under the action of an encoding gradient G_e. Such pulse will impart a parabolic phase on the spins, $\Phi_e(y) = \alpha_e y^2 + \beta_e y + c$, in which y is assumed to be the encoding gradient's axis. Due to this parabolic profile the collected signal will be dominated by spins located at the stationary point fulfilling $[\partial\Phi/\partial y] = 0$; i.e., by regions where the spins' accrued phases change slowly (18). Although this condition will be initially fulfilled solely at $y_o = -\beta_e/2\alpha_e$, this stationary point can be displaced by application of additional gradients. Spatiotemporal-encoding MRI time-domain signals are thus acquired while under the action of an acquisition gradient G_a, which moves the stationary point throughout the FOV, rasterizing the NMR profile being sought over an acquisition time T_a. This approach to scanning 1D axes can be extended into single-shot 2D MRI experiments by executing it in a so-called "hybrid SPEN" fashion, whereby an orthogonal readout (RO) domain is imaged in a usual *k*-space fashion by the incorporation of a second, rapidly oscillating gradient. The ensuing sequence carries an evident resemblance to spin-echo echo-planar imaging (SE-EPI) (Fig. 1), but provides the possibility of imaging the latter's low-bandwidth domain without the limitations of Fourier sampling. This enables the use of stronger gradients than in EPI-based counterparts; it also opens the possibility to perform a "full refocusing", whereby spin-packets echo continuously throughout the course of T_a, rather than at a single instant as in a normal SE (19,20). For this full-refocusing condition to hold the acquisition gradients and times have to fulfill $T_e = T_a/2$ and $|G_e| = |G_a|$ for an inversion-based encoding, or $T_e = T_a$ when relying on a chirped excitation (this difference stems from the additional factor of two introduced in the phase by a swept inversion pulse over an excitation counterpart of equal bandwidth) (21). These possibilities of using stronger gradients, and of refocusing T_2^* effects throughout the acquisition, have been shown to aid in the performance of single-scan MRI experiments at high fields, or when targeting challenging areas in animal or human anatomies (6–8,22–26).

F1

[1]Department of Chemical Physics, Weizmann Institute of Science, Rehovot, Israel.

[2]Department of Electrical Engineering and Computer Sciences, University of California, Berkeley, California, USA.

Financial support was received from the Israel Science Foundation (Grant No. 795/13), the EU through ERC-2016-PoC (Grant No. 751106), Minerva funding (Grant No. 712277) from the Federal German Ministry for Education and Research, the Kimmel Institute for Magnetic Resonance, and the generosity of the Perlman Family Foundation. M.L. also acknowledges the Weizmann Institute for a Visiting Faculty Program Fellowship.

*Correspondence to: Prof. Lucio Frydman, Department of Chemical Physics, Weizmann Institute of Science, 205 Herzl Street, Rehovot 76100, Israel. Tel: +972-8-9344903; E-mail: lucio.frydman@weizmann.ac.il.

Received 29 January 2017; revised 2 April 2017; accepted 3 April 2017
DOI 10.1002/mrm.26731
Published online 00 Month 2017 in Wiley Online Library (wileyonlinelibrary.com).

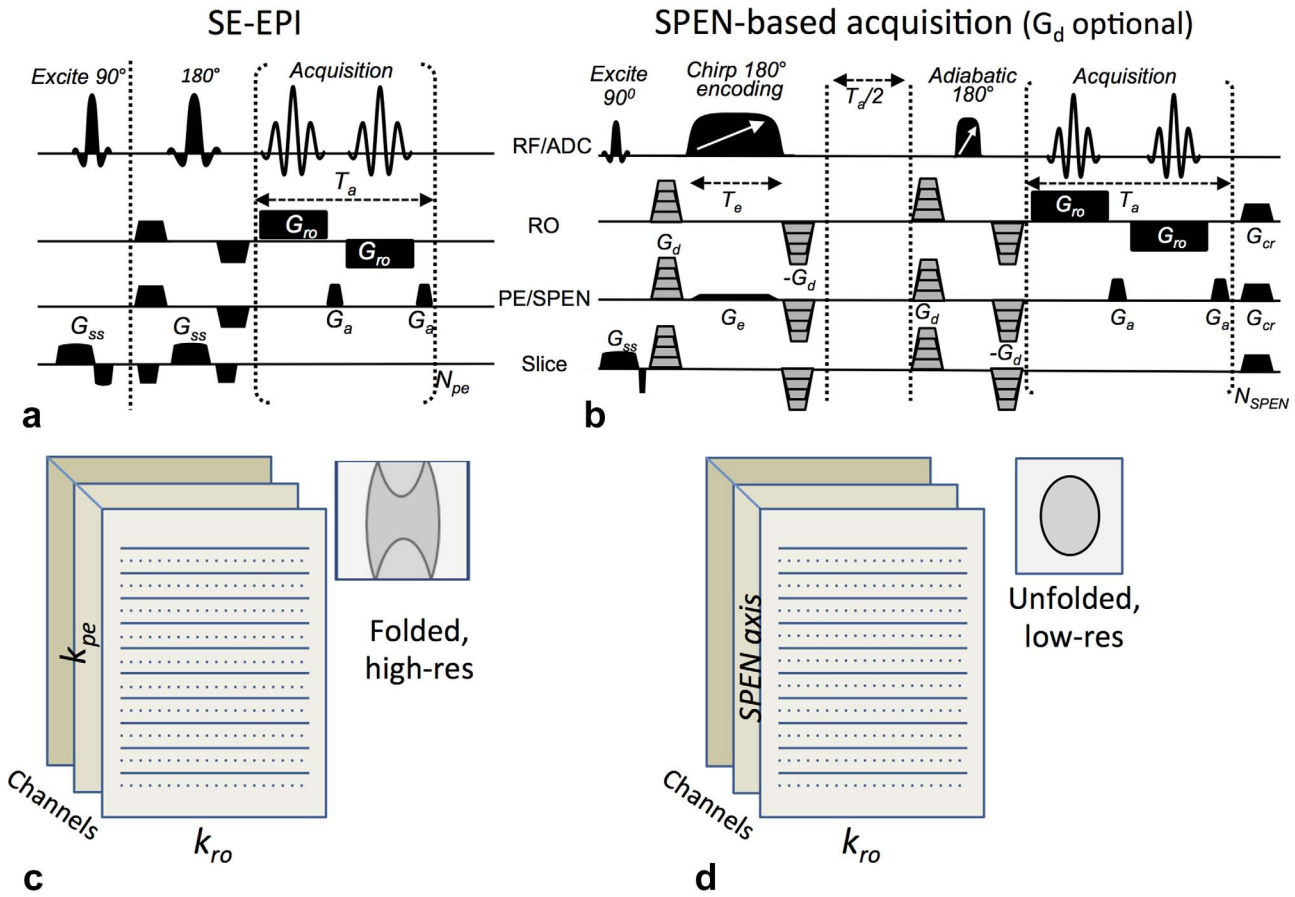

FIG. 1. **a, b**: Pulse sequences for SE-EPI and hybrid SPEN. The latter involves an initial 90° slab-selective excitation, a pre-encoding $T_a/2$ delay inserted to achieve full-refocusing conditions, a 180° chirped encoding pulse, and a postacquisition adiabatic 180° pulse that returns all spins outside the targeted slice/slab back to thermal equilibrium (20). Optional doubly refocused diffusion-weighting gradients G_d in-between the 180° pulses are shown for diffusivity mapping; diagonal arrows indicate frequency modulations on the corresponding pulses. Additional abbreviations: RF/ADC, radiofrequency and analog-to-digital conversion channels; cr, crusher; sp, spoiler. **c, d**: Differing effects of skipping lines (dashed) in the low-bandwidth domains. Whereas in EPI this leads to folding artifacts that require multiple sensors for unfolding and require either additional autocalibration lines (31) or independent acquisitions to obtain the sensitivity maps, in SPEN they lead to lower-resolution but unfolded images, which can be improved by super-resolution procedures and used directly for sensitivity-map calculations.

Despite these advantages, SPEN faces a number of sensitivity versus resolution challenges. Spatiotemporal encoding's resolution is in principle given by α_e, which reflects the steepness of its parabolic phase. Imposing a tight parabola will achieve high spatial resolution yet at the expense of sensitivity, an onerous cost given SPEN's non-Fourier nature. Loosening the parabola sacrifices resolution but reinstates an EPI-like sensitivity, while simultaneously lessening power deposition (specific absorption rate, SAR) requirements (27). Moreover, it has been shown that the use of super-resolution (SR) and of other postprocessing algorithms (4,7–10,23) can make up for these resolution losses, provided that the sampling occurring along the SPEN axis is sufficiently dense. In single-shot 2D SPEN (Fig. 1b), however, instances will often arise in which the resolution and FOV conditions desired along the readout will not allow a sufficiently dense sampling along the SPEN acquisition domain. Recently, Schmidt et al described a way of alleviating this, based on the acquisition of multiple interleaved scans (28). Unlike interleaving in EPI, where small subdwell Δk "blips" increase the sampling density so as to faithfully cover the targeted low-bandwidth FOV and thus avoid folding (29,30), SPEN interleaving aims to improve the spatial resolution by sampling regions in space, which would otherwise be skipped by the sampling parabola (Fig. 1, lower panels). This presents advantages vis-a-vis EPI's interleaving, including the delivery of full-FOV images for every interleaved scan, and thereby the option of carrying out the procedure in a self-referenced, image-based fashion (28). Still, as depicted so far, both interleaved EPI and SPEN share the common need for performing multiple scans for improving the images being sought, thus forfeiting the original, single-shot nature of these experiments.

The present study explores the possibility of achieving an oversampling that is identical to that afforded by interleaved SPEN, while confining the experiment to a single scan. This possibility arises from the use of multiple receiving coils. Parallel imaging is used widely in

MRI as a way of enlarging the targeted FOV, without complying with the full criteria imposed by Nyquist sampling (29–32). Parallel acquisition methods have also been used in SPEN to enlarge the FOV while shortening the acquisition time, by using multiband swept pulses targeting regions that are associated with different receiving coils (3,33). It is interesting to note the differences between these two approaches to exploit the availability of multiple receivers, as these stress the distinct principles that these acquisitions exploit to deliver their images. In simultaneous acquisition of spatial harmonics (SMASH), sensitivity encoding (SENSE), or generalized autocalibrating partially parallel acquisition (GRAPPA), the sensitivity of different coils to different regions in space is used to effectively fill skipped *k*-points, and thereby avoid undesired fold-overs (Fig. 1a, lower panel). In SPEN, the availability of coil-resolvable regions in space has been used to expand the FOV by simultaneously encoding multiple adjacent volumes using multiband chirp pulses, and unraveling these by independent sensors. There is, however, an unexplored option to improve the latter experiment by parallel receiving, and stems from viewing the SPEN acquisition as a sampling occurring not just in real but also in *k*-space. In this scenario, the resolution enhancement arising after implementing SPEN image interleaving can also be visualized as involving the collection of additional scans filling in-between samples in a *k*-space grid. Unlike what happens in regular MRI, these *k*-blips will only contain contributions that are spatially limited by the parabolic encoding. As a result of this local encoding nature, filling up these "missing" points does not result in a global image unfolding; instead, it provides a potential resolution enhancement that is entirely analogous to that arising by the SPEN interleaving procedure. One can therefore envision relying on similar algorithms as used in SMASH or SENSE, to extract this additional information; SPEN's localized nature, however, implies that these reconstructions will be much less demanding than their regular *k*-sampling counterparts. The principles of this SPEN-oriented reconstruction algorithm are described in the following section based on more familiar SMASH and SENSE arguments; we then present phantom and in vivo results collected on a clinical head setup that illustrate the ensuing super-resolved SPEN with SENSE (SUSPENSE) resolution enhancement, including the methodology's potential to deliver quality single-shot brain diffusion maps at submillimeter resolutions. Furthermore, a number of additional pulse schemes are incorporated into SUSPENSE, which enable it to achieve these resolutions over FOVs, SARs, and repetition times (TRs) that are equal to state-of-the-art EPI values, while benefiting from SPEN's additional robustness to field heterogeneities. An analysis of SUSPENSE's sensitivity compromises on the basis of g-factor mapping arguments, is also presented.

METHODS

The SUSPENSE Algorithm

As mentioned, the SPEN signal can be visualized as either a *k*-domain acquisition whose signal *S(k)* is detected under the action of an acquisition gradient G_a, or as a direct spatial-domain acquisition over a time T_a of the image being sought, i.e.,

$$S[k(t)] \propto \int_y \rho(y) e^{i[\varphi_e(y)+k_{pre}y+\gamma G_a y t]} dy = \int_y \rho(y) e^{i[\varphi_{total}(y)]} dy \approx \Delta y \cdot [\rho(y_{stat})] \left(\frac{\partial \varphi_{total}}{\partial y}\right)_{y=y_{stat}}=0 \quad [1]$$

where k_{pre} is a suitable prephasing gradient that defines the beginning of the rasterization ($-\gamma G_a T_a/2$ in the case of encoding by an inversion pulse), and y_{stat} is the coordinate that for a given $k(t) = \gamma G_a t$ ($0 \le t \le T_a$) fulfills the stationary phase condition. Assuming that signals are monitored over a suitable time T_a (usually $2G_e T_e/G_a$ for an inversion-based encoding), the $[\partial\Phi/\partial y] = 0$ condition implies that $|S(k)|$ will be proportional to the $\rho(y)$ profile at uniformly spaced locations: $y(k) = -FOV/2 + k*FOV/(\gamma*G_a*T_a)$. Extension of these arguments to a 2D hybrid SPEN acquisition requires retaining a discretized SPEN version of Equation [1], which assuming the digitization of $1 \le m \le M$ points leads to

$$S[k_m] \propto \sum_n \rho(y_n) e^{i[\varphi_e(y_n)+k_{pre}y_n+k_m y_n]} \quad [2]$$

where $1 \le n \le N$ is an index denoting the center of the y_n^{th} voxel. As in EPI, the sampled values of k will usually be equispaced, $k_m = (m-1)\Delta k_{SPEN}$; unlike in EPI, however, these Δk_{SPEN} values will not be given by Nyquist criteria. Instead, they will be defined by the bandwidth $BW = \gamma G_e FOV$ of the swept pulse used to impart the spatiotemporal encoding, by the duration T_e of this pulse, and by the number M of sampled blips. The chirped bandwidth in SPEN is usually set so that the hertz/pixel in the final image is sufficiently large to overcome field inhomogeneity distortions-normally 2 to 5 times stronger than for the low-bandwidth axis in a comparable EPI acquisition (alternatively, should these factors be set equal, there would be little point in performing SPEN rather than EPI). Bandwidth times the encoding time T_e, also referred to as the pulse's time-bandwidth product $Q = BW \cdot T_e$, dictates together with the FOV the curvature of the SPEN-encoding parabola: $\alpha_{enc} = -Q/FOV^2$. Q therefore defines the resolution that can be obtained from a simple magnitude calculation of the data. In addition, Q will define the number of elements that should ideally be acquired to separate all of the resolvable spatial elements in the SPEN image. Indeed, for the fully refocused sequences to be considered, where isochromats span a bandwidth of frequencies, the ideal dwell time Δt of a SPEN sampling that aims to capture all spatial features would have to fulfill: $\Delta t = 1/(2BW)$. If this sampling is implemented by M_{ideal} points spread over an acquisition time T_a, this in turn indicates that $T_a/M_{ideal} = 1/(2BW)$ or, in other words, $M_{ideal} = BW \cdot T_a = 2Q$. This represents the ideal sampling that one would like to fully capture the available resolution. Collecting this many points will generally be feasible for unconstrained, 1D acquisitions. However, for 2D single-shot sequences of the kind introduced in Figure 1, in

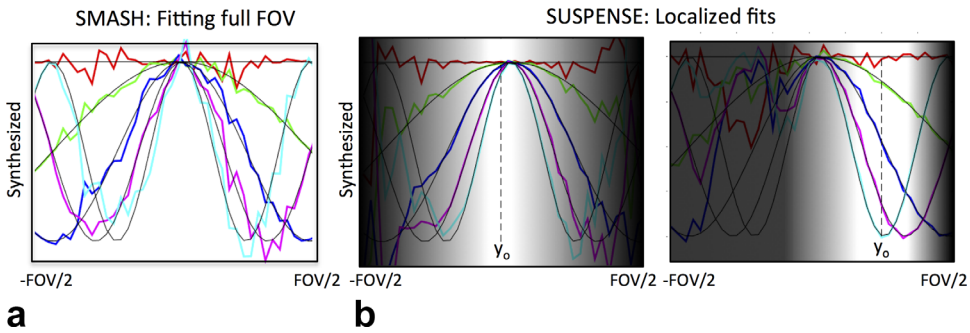

FIG. 2. Comparison between sensor-synthesized harmonics in conventional *k*-space imaging (**a**) and locally accurate sensor-synthesized harmonics of the kind used in this study (**b**) to interleave SPEN data. Different coefficients are used to synthesize a desired set of harmonics around the two different y_o locations shown (brightest region in panels), with zeroth-to-fourth harmonics shown in different colors.

which SPEN needs to include gradient oscillations encoding the orthogonal k_{ro} domain, acquiring this many samples will not be generally possible unless restricting the range of experimental k_{ro} values, using exceedingly long echo times (TEs), or relying on inordinately rapid and intense G_{ro} gradients. As mentioned previously, such dense subsampling can be recapitulated by the interleaving procedure introduced in (28). Spatiotemporal encoding interleaving makes up for undersampling by applying a suitable set of blips that advance the overall spatial sampling carried over N_{shot} independent scans, in increments of $\Delta k_l = (l-1)(\Delta k_{SPEN}/N_{shot})$, $l = 1 \ldots N_{shot}$. In a suitably interleaved experiment, the number of sampled points M_{spen} times N_{shot} will then equal $2Q$.

Remarkably, the availability of multiple receivers sampling different regions throughout the targeted FOV provide the means to compute the signals that would arise from multiple interleaved SPEN scans, in a single signal acquisition. To visualize how this is feasible, we recall that according to the SMASH formalism (30), spatial phase variations can, if sufficiently slow, be mimicked by summing signals arising from multiple coils: $\exp[-ih\cdot\Delta k\cdot y] = \sum_c n_c^h(y) S_c(y)$, where $n_c^h(y)$ are suitable weighting coefficients for the hth harmonic, and $S_c(y)$ are sensitivity maps for the various *c*-coils. Such formalism can be of limited usefulness, as the weighting coefficients need to hold throughout the entire FOV_y (Fig. 2a); in contrast, in SPEN, where signals are emitted from localized spatial neighborhoods, it is simple and robust to extend such formalism for the sake of computing the "missing" interleaved data in a localized manner. To do so, we look for a set of localized coefficients $n_c^h(y)(x', y')$ such that the coils will satisfy for a particular (x', y') neighborhood

$$\sum_{c=1}^{N_c} n_c^h(x', y') W(y) S_c(x, y) = W(y) \exp[-ih\Delta k_{SPEN} \cdot y / N_{shot}] \qquad y \in FOV \qquad [3]$$

where N_c is the number of coils and $W(y)$ is a weighting function that emphasizes the local nature of the SPEN interpolation. For this function we used a Gaussian centered at the y' position being considered and weighted by a $\sigma = 1.2$, as this was found to be the best tradeoff between resolution and artifacts (lower σs led to smoother lower resolution images, whereas higher σs led to a higher resolution albeit enhanced artifacts). This local interpolation enables one to faithfully synthesize localized harmonics up to a degree $R \leq N_c$ (Fig. 2b), leading to a resolution enhancement factor that takes the role that N_{shot} played in the interleaved acquisitions. This *R*-factor multiplies the effective number of points collected along the SPEN axis, increasing it from $2 \cdot M_{spen}$ to $2 \cdot R \cdot M_{spen}$. For a good parallel receiving setup, it is sensible to increase this number up to $M_{ideal} = 2 \cdot Q$. At this limit, the effective oversampling has covered the maximum range of bandwidth frequencies contained by the targeted FOV. Sampling a larger bandwidth (i.e., interpolating further in *k*-space) will improve the nominal resolution, but will neither enhance the actual spatial resolution nor lead to any additional improvements by SR algorithms. In fact, at this full sampling limit, the SPEN experiment can be viewed as a conventional *k*-space acquisition on an object that has been imparted a priori with a quadratic phase. Thus, the object's reconstruction can be carried out by a simple Fourier transform (FT), without a need to carry out what may sometimes be an ill-conditioned SR reconstruction.

One appealing aspect of this coil-based interpolation procedure is that, unlike what occurs when physically collecting interleaved SPEN scans or performing parallel *k*-based imaging, the value of *R* can be set and changed during a processing stage, until optimal images arise. In other words, the role taken by this *R*-factor is entirely akin to that played by the undersampling ratio in parallel imaging schemes—apart from the fact that its value can be chosen and optimized after completing, rather than before beginning, the acquisition. Another appealing difference between this SPEN resolution enhancement and *k*-space acquisitions relates to the fact that, like all parallel imaging approaches, SUSPENSE requires a priori knowledge of the coil sensitivity maps $\{S_c(x,y)\}_{1 \leq c \leq Nc}$ to be used. The direct-space sampling nature of SPEN, however, implies that despite its low-bandwidth undersampling, all of its preprocessed images are free from folding effects. The single-shot image to be interpolated therefore carries each coil's individual, unfolded sensitivity map; to extract these, one can either calculate ratio images between each channel's signal (after smoothing) and the total root mean square (RMS) image, or rely on an algorithm like Eigenvalue-based

self-consistent parallel imaging reconstruction (ESPIRiT) (34). In the present study, we used both approaches and, in either case, the coil mapping remained fully self-referenced and autocalibrated.

Although Eq. [3] implements the k_{SPEN}-space interpolation based on the SMASH formalism, it is feasible to carry out an essentially equivalent resolution enhancement procedure by SENSE-based reconstruction algorithms (29,32). In this case, one would then search for an image ρ satisfying $A\rho = S$, where A is an operator that includes a convolution by the quadratic phase that SPEN imparted on the spins, a weighting on the multiple sensors' sensitivities, and an FT implemented along the RO direction in the case of 2D hybrid acquisitions. Because of numerous missing SPEN/k-lines, searching for a high-definition ρ image based on a direct inversion of $S = A\rho$ would lead to folding. Therefore, an alternative approach was adopted in which a high-resolution, regularized image ρ is sought that, after subject to a correct transformation described by the A operator, reproduces the measured signal. This A is an image-to-data transformation operator; therefore, in this case it involved multiplication by the various coils' sensitivity maps: FT along the RO dimension and multiplication by a suitable SR matrix along the phase-encode dimension (4,10) (for the multiband experiments introduced below A also included summing over the contributions from the different bands). To guide this search in image space, the nonlinear conjugate gradient algorithm in (35) was adopted, using a sparse image representation based on a wavelet transformation and total-variation regularization in the image search.

Experimental Methods

Experiments were performed on a 3T Siemens TrioTIM (Siemens Healthcare, Erlangen, Germany) scanner using a 32-channel head-only coil. Phantom experiments to ascertain the resolution enhancement were run on a Bruker stripped phantom (12-cm diameter; ~0.8 mm between stripes). Brain imaging scans were run on healthy volunteers in a protocol that included the acquisition of turbo spin-echo reference images, SE-EPI images (Fig. 1a), and multislice SUSPENSE scans using the sequence in Figure 1b with/without the diffusion gradient weighting, as determined by the experiment. This sequence was implemented using doubly refocused and fully refocused formats that have already been described (19,20,36), but it included a number of innovations to increase volume coverage that are worth mentioning. One of these involved the use of stimulated echoes capable of delivering numerous slices for each encoded slab (20,36). Another modification included the use of multiband pulses addressing different regions along the slice-selection (z) axis, chosen distant enough to have different sensors in charge of their bulk detection (39). These multiband pulses were written as sums of simple *sinc*s with Hamming windowing, and were 2.5 to 5 ms long; no provisions were taken to optimize the SAR of these pulses. The parallel-receive axis exploited by these pulses lies perpendicular to the one discussed previously in connection to SUSPENSE, and to its Δk_{SPEN} interpolation along y. Still, in these simultaneous multislice experiments, an additional constraint was added to the system of equations in Equation [3], requiring that for each band the contribution of all other bands be zero. Mathematically, this was cast as

$$\sum_{c=1}^{N_c} n_{c,m}^{h}(x',y')W(y)S_c^{m'}(x,y) = 0, \quad y \in FOV\,, m \neq m' \quad [4]$$

where $S_c^m(x,y)$ is the sensitivity map for the mth slice, and m' encompasses all other slices that were simultaneously excited together with one being processed. Finally, to facilitate the simultaneous acquisition of multiple nearby slices in a single scan, an approach analogous to EPI's simultaneous image refocusing (SIR) (37,38) was also implemented. In this approach, a "k_{ro} kick" is applied in between subsequent excitation pulses, leading to multiple slice-specific echoes being resolved during each oscillating readout segment. As the SAR in multislice SPEN stems predominantly from the application of the swept 180° encoding pulses in the sequence, all of these procedures enabled us to widen the volume covered, without a concomitant increase in SAR. Typical SUSPENSE acquisitions thus managed to cover 20 × 18 × 7.2 cm volumetric FOVs at 1 × 0.9 × 3 mm spatial resolutions, with TE ≈ 50 to 90 ms and TR = 3 s. In all these volumetric studies, SAR values ranged between 60 and 90% of the scanner's maximum prescribed values for brain analyses. Diffusion-weighted imaging maps were also run on volunteers by adding suitable sensitizing gradients (26,39), and compared against EPI scans collected using a scanner-supplied twice-refocused SE-EPI sequence (34). All studies were approved by the institutional review board of the Wolfson Medical Center (Holon, Israel), and signed, informed consents were obtained from all of the participants.

Data Processing

To implement the SUSPENSE image reconstruction, in-house algorithms were written in MATLAB (The MathWorks, Natick, MA); all other images were processed on the scanner. When relying on SIR to encode multiple slabs along the slice-selection axis, the data for each echo were first separated using a simple splicing along the k_{ro}-space. In single-band protocols, sensitivity maps could be extracted directly from the same data set as used for the actual imaging. For this, standard SR was used to extract a well-resolved image per channel, from which sensitivity maps were calculated using either the ESPiRiT algorithm (34) or from the ratio between the smoothed images arising from each channel and the overall RMS image. In multiband runs this self-referenced procedure was not suitable, and sensitivity maps had to be obtained from separate acquisitions. These separate acquisitions used identical parameters as the subsequent SPEN runs, apart from the use of conventional rather than multiband pulses. To make up for this change, the number of collected slices was naturally increased, and with it increased the overall TR. Using these sensitivity maps, two approaches were developed to reconstruct the final high-resolution image—both

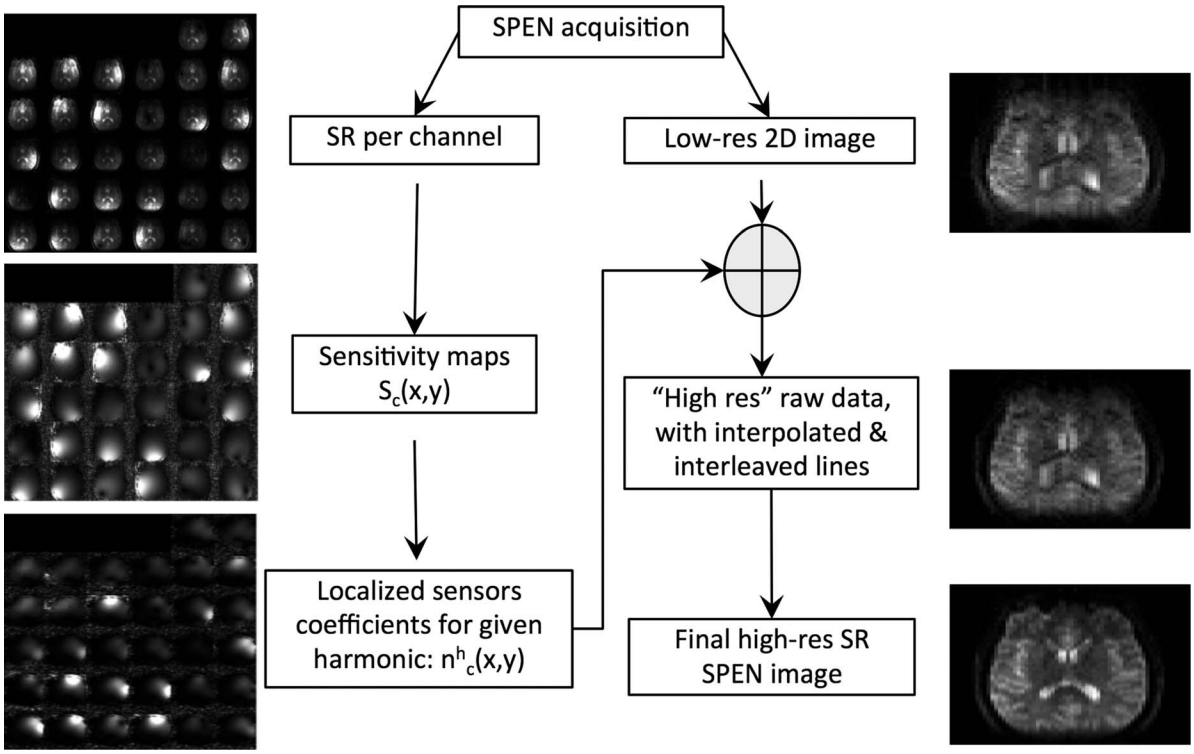

FIG. 3. Basic algorithm for interpolating single-shot SPEN data in its *k*/image space, based on manipulations that synthesize the missing data from higher-order coil harmonics. The left-hand side describes the procedure used for obtaining the coefficients maps for a given set of spatial harmonics, based on channel-per-channel SR-enhanced images leading the sensitivity and coefficient maps being sought. The right-hand column shows how these coefficients permitted a reconstruction of the missing lines, leading to a substantial resolution enhancement at no extra experimental cost. See the main text for an alternative, image-based reconstruction algorithm.

yielding results of similar qualities. In the first one, the missing SPEN lines were calculated by locally combining the data from the different sensors (Eq. [3]), calculating the required coefficients for the higher-order harmonics using a Moore-Penrose inverse of the constraints matrix with a small Tikhonov regularization ($\lambda = 0.001$). These coefficients were calculated for each (x, y, z) location (see Fig. 2 for calculations for particular (x_o, z_o) coordinates), and g-factor maps (29) were calculated for each location and each harmonic. With the aid of these harmonics, the missing lines in the SPEN data set were reconstructed, and the final image was calculated using the super-resolution algorithm described in (23) on the resulting augmented set. In an alternative rendering of this processing, an image-based SENSE reconstruction procedure was implemented using the nonlinear conjugate gradient algorithm in (35) with total-variation regularization. This algorithm required implementing image-to-data transformations (and their conjugate transform), which for the hybrid SPEN acquisitions required (i) the application of an appropriate parabolic phase, (ii) an FT along the RO dimension, and (iii) suitably accounting for the different channels sensitivities. The code for the ensuing SUSPENSE algorithm is available upon request. For the diffusion experiments, apparent diffusion coefficient (ADC) maps were calculated voxel-wise from the data measured using a $b_0 = 0$ and three $b = 650$ s/mm^2 values achieved by orthogonal diffusion-weighting gradients. Additionally, when multiple scans where averaged to improve the sensitivity of diffusion measurements, an L_2 regularization was used to enable the averaging of the single-shot SPEN data in image space; this averaging was rendered free from phase complications and instabilities, by performing it either in magnitude or after a low-resolution phase correction of the 2D images.

RESULTS

Figure 3 summarizes the main steps used in the resolution-enhancing procedure introduced in this study, using actual single-slice brain data as the illustration. The procedure begins by resolving the various slices and FT of the data along the k_{ro} axis, to yield for a given slice a set of low-resolution 2D images per sensor. The quality of these raw images is improved using a super-resolution algorithm (Fig. 3, left-hand column), and from these improved images the sensitivity maps $\{S_c(x,y)\}_{1 \le c \le Nc}$ are obtained as detailed in the "Methods" section. Solving Equation [3] for each location allows one to obtain the desired spatially dependent coefficient maps, as illustrated in the lower-left panel of Figure 3 for $h = 2$. These coefficients are then used to complete the missing data lines (Fig. 3, center-right panel), and a super-resolution procedure on the resulting set involving a deconvolution with the quadratic phase kernel yields the high-definition image being sought. Notice that this final full image (Fig 3, lower right) is obtained by implementing an RMS combination of the different sensors' data,

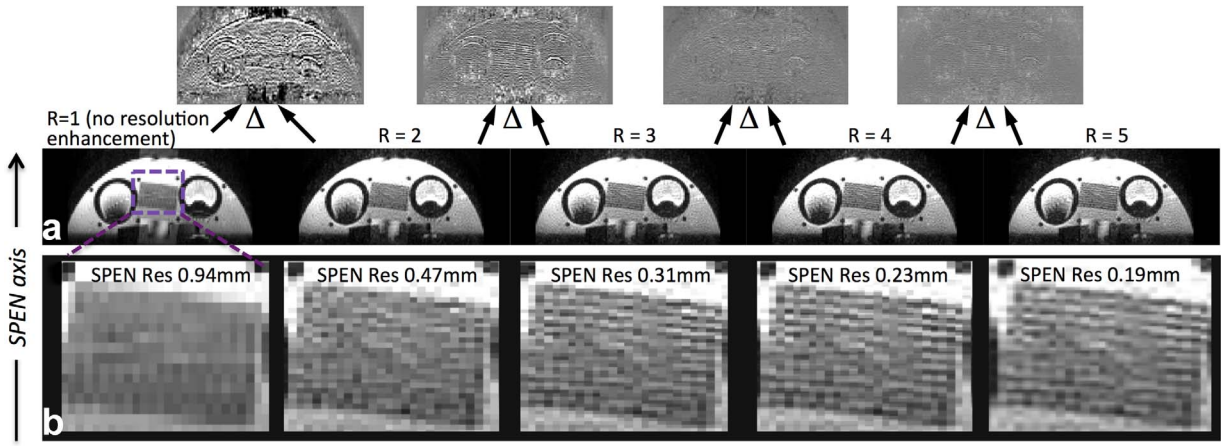

FIG. 4. Resolution-enhanced processing of phantom-based SPEN data. **a**: Single-shot phantom images processed with different reconstruction enhancements as summarized in Figure 3, using R factors ranging from 1 to 5. Basic acquisition parameters: FOV = 15 × 4.5 cm, SPEN $Q = 65$, $G_e = 0.1$ G/cm, $T_e = 31.7$ ms, and $M_{spen} = 48$, in-plane matrix size after SR = 200 × 48 (i.e., 0.75 × 0.9375 mm resolution). **b**: Zoomed-in images show the improvement achieved by the processing onto a high-spatial-frequency portion of the phantom as the nominal SPEN-axis resolution drops well below 1 mm. Shown on top of the figure are difference (Δ) images between consecutive renderings of the data, indicating the absence of changes/improvements past R ≈ 3.

yielding—as happens in the case of generalized autocalibrating partially parallel acquisition (32)—a concurrent improvement in signal-to-noise ratio.

F4 Figure 4 shows the effects of this procedure on single-shot SPEN results collected on a phantom, in which the SPEN axis is placed along the vertical dimension. This phantom possesses a number of carved features, including a stripped structure with slots spaced by ~0.8 mm. Although all of the images shown were obtained from the same single-scan data set and processed using super-resolution, their definitions along the SPEN axis are clearly different. This can be appreciated by comparing the slotted blowouts shown on the lower row of the Figure. Notice that although additional *k*-rows can be interpolated up to the number of available receiver coils, the images show no resolution improvements past a R ≈ 3 factor. This can be appreciated in the images as well as by the differences calculated between consecutive interpolation steps, shown on the top row of Figure 4. This is in agreement with the previously mentioned expectations, whereby extending the oversampling beyond 2Q (130 for this phantom) does not lead to an actual spatial-resolution improvement, but simply to a data interpolation.

F5 Figure 5 illustrates further the details of this procedure, using a volunteer brain scan as an example. Stimulated-echo SPEN allowed us to cover a whole-brain FOV of 20 × 18 × 7.2 cm with 24 slices in 3 s (for the sake of stressing the processing details, these images are shown after signal averaging 80 identical scans in image space). The original resolution of the SPEN acquisition was set to 1 × 4.5 × 3 mm along the RO/SPEN/SS dimensions, using $M_{spen} = 40$ samples. Figure 5a shows a representative slice arising after super-resolution of these data without SUSPENSE; Figure 5B shows the same slice after SUSPENSE is implemented with R = 5, leading to the effective sampling of all 2Q = 200 values associated with the acquisition. The resolution improvement along the SPEN axis is evident, even if there is a noticeable "stripping" when comparing it against a multiscan turbo spin-echo counterpart collected at a similar 1 × 1 × 3 mm resolution. We traced this artifact to residual even/odd effects that remain to be corrected in the SUSPENSE acquisition. Figures 5d and 5e present additional aspects of this multicoil processing, including the sensitivity maps $\{S_c(x,y)\}_{1 \le c \le 32}$ (magnitude and phase) afforded by ESPIRiT from the original SPEN images, and the $\{n_c^{h=2}(x,y)\}_{1 \le c \le 32}$ spatial coefficients obtained from the sensitivity maps for the second spherical harmonic set required for implementing R = 5 SUSPENSE (only the first five channels are shown for clarity). From the first of these data sets, g-factor maps can be calculated that describe the degree of independence of the various sensors. Noise amplification factors were calculated from these g-factor maps, using a multiple-replica approach in which synthetic noise with a priori known statistics was artificially fed throughout the targeted FOV, and its value at the conclusion of the SUSPENSE processing was evaluated. Figure 5f illustrates the ensuing noise maps for R = 5 interpolations executed using the SENSE algorithm.

As mentioned in the theoretical considerations, as the number of sensor-interpolated points increases, the gains that can be conveyed by subjecting SPEN data to super-resolution vanish. Figure 6 illustrates this by comparing, F6 using the same data set as introduced in Figure 5, the results that can be retrieved for R = 15, upon applying the SR versus a conventional FT along the interpolated axis. The virtual identity between the two images reflects the fact that, for a sufficiently dense and accurate interpolation, the entire frequency range that was involved in the SPEN acquisition—as given by the bandwidth of the FOV that was encoded by the chirp pulse—becomes faithfully characterized by SUSPENSE's oversampling. This shows that, given a sufficient interpolation, all complications associated with SPEN's postprocessing methods can be bypassed without relinquishing on SPEN's immunity to inhomogeneities.

Figure 7 illustrates the SENSE-based interpolation F7 algorithm using a diffusivity measurement as test. To

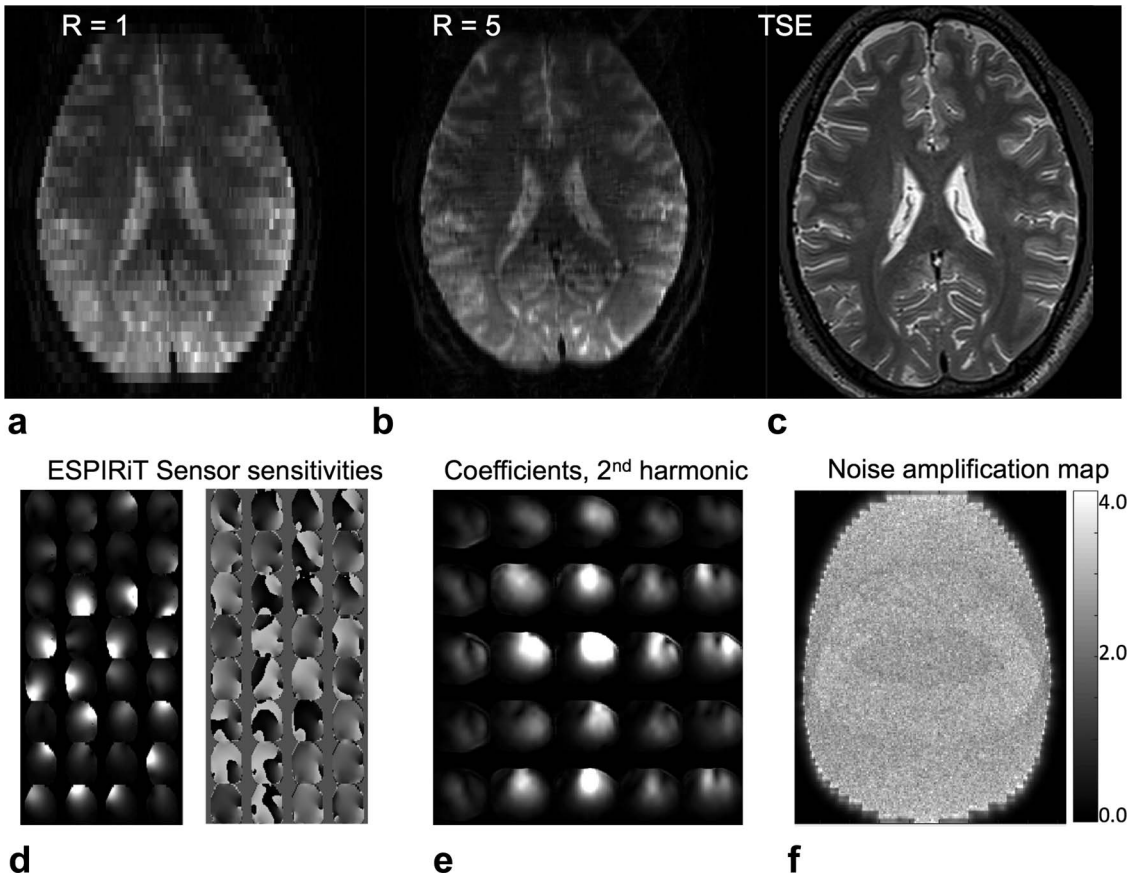

FIG. 5. **a, b**: Same as in Figure 4 but for acquisitions performed on a human volunteer, for an in-plane FOV of 20 × 18 cm. The initial resolution of 1 × 4.5 mm was improved to 1 × 0.9 mm with an R = 5 factor, chosen to fulfill $M_{spen}.R = 2Q =$ 200 (as $T_e = 20$ ms, BW = 5 kHz). To better show SUSPENSE's resolution improvements, these images arise from averaging 80 identical, separately processed repetitions. **c**: Turbo spin-echo anatomical image collected at 1 × 1 mm in-plane resolution. Additional aspects of this processing approach include magnitude and phase-sensitivity maps derived from ESPIRiT (**d**), some of the coefficient maps calculated for $h = 2$ (**e**), and a noise amplification map calculated for R = 5 SUSPENSE (**f**). The latter estimation was calculated using a synthetic-noise multiple-replica approach, followed by SUSPENSE reconstruction based on the SENSE algorithm with a linear, norm-2 regularization. Minor ghosting artifacts visible in the R = 5 image reflect departures from the stationary phase approximation (8).

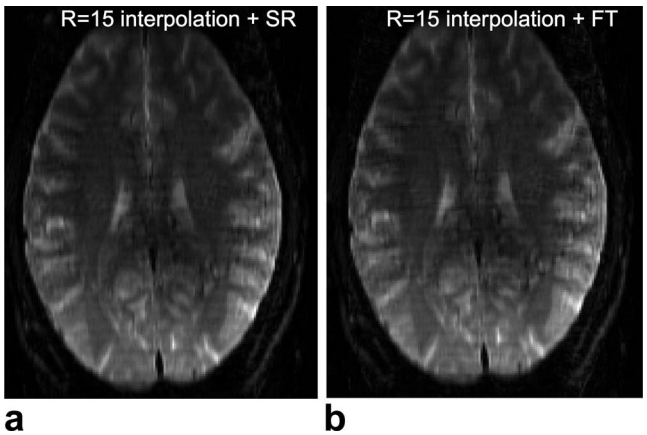

FIG. 6. Consequences of a very high *k*-space SPEN interpolation: As the spatial voxel size after using a high R-value (in the present case, 15) becomes very small, the intravoxel dephasing as a result of the quadratic phase weakens. Hence, one obtains a similar result by approximating the image ρ using the super-resolution procedure of Figure 2 or by a simple $\rho \approx FT[S(k_{SUSPENSE})]$ transform (the resulting image then contains a quadratic phase, not seen in these magnitude-mode displays).

implement the latter, pairs of doubly refocused diffusion gradients were applied along orthogonal axes in different scans (Fig. 7a). These results illustrate an attractive feature of the ensuing approach: Given SUSPENSE's robustness this procedure can be implemented on a scan-by-scan basis, and the resulting images co-added in magnitude mode without suffering from phase inconsistencies. This in turn endows excellent sensitivity to the final diffusion maps, despite their submillimeter resolution. Comparisons against conventional EPI-derived ADC maps (Fig. 7b) clearly illustrate these resolution improvements, while certifying the correctness of the SUSPENSE diffusion maps when compared against single-shot counterparts. Additional data provided in the Supporting Information (Supporting Figs. S1 and S2) demonstrate the possibility of retrieving this kind of high-definition data with a rapid and sizable volumetric coverage, while retaining low SAR values.

DISCUSSION AND CONCLUSIONS

This study introduced a new approach for improving the resolution of hybrid SPEN acquisitions, at no expense to

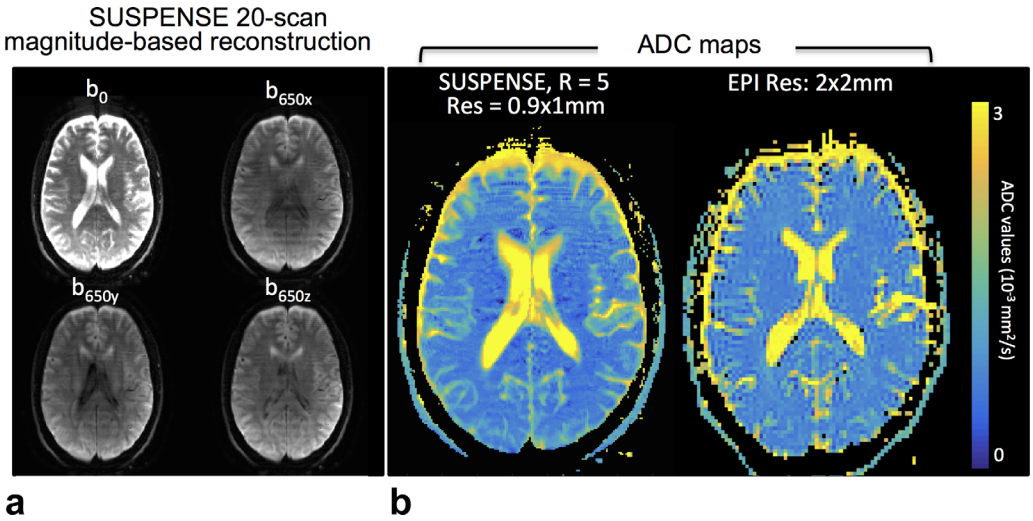

FIG. 7. Diffusion-weighted brain images illustrating the quality achievable by combining the SUSPENSE single-shot sensor-based interpolation with multiscan averaging. **a**: R = 5 SUSPENSE *b*-weighted images arising after 20 averages, collected using the indicated nominal *b*-values. Images (13 slices) were originally acquired with a 20 × 20 × 10.4 cm FOV and a 4.5 × 1 × 2 mm resolution. Total experimental time = 14 min. **b**: Comparison between the ADC maps arising from the interpolated SUSPENSE versus EPI experiments collected on the same FOV—the latter with a 2 × 2 × 2 mm spatial resolution. Notice that despite the uneven T_2 contrast evidenced by the SPEN images as a result of the sequential image unraveling along the anterior to posterior direction, this effect factors out after computing a normalized contrast like diffusivity. In this case, SPEN images were processed using a SENSE-based reconstruction. The EPI map arises from a four-scan signal-averaged acquisition lasting approximately 1 min.

experimental complexity or increase in acquisition scans. This opportunity stems from the realization that in SPEN the acquisition wave vector plays a dual role: delivering at the same time the image in direct space, while sampling a reciprocal space. Image interleaving procedures that had been performed in multiple scans could then be replaced by *k*-space interpolation procedures based on multiple receivers. This delivered higher-resolution images at no additional expense to the experimental protocol, using information that until now had not been exploited in this kind of acquisition. The approach is certainly not general, as it requires a sufficiently high number of independent sensors—a commodity that is rarely available in preclinical settings, and not always efficiently implemented in human scanners. When parallel imaging facilities are available, however, SUSPENSE's images exhibit substantially better resolution than their SPEN counterparts. Furthermore, with the highest g-factors observed for the highest harmonics remaining less than or equal to 3, reasonable signal-to-noise ratio losses are associated with this increased resolution. Another attractive feature is the method's self-referenced, autocalibrated nature. This full self-reliance opens the possibility of averaging signals using magnitude-mode, direct-space, single-shot images—even when involving diffusion-weighting gradients. This in turn enables the acquisition of high-resolution and high-sensitivity ADC maps, as illustrated in Figure 5. A third notable feature of SUSPENSE is the possibility of reconstructing its higher-definition images in a variety of ways. In the present case we demonstrated approaches based on the synthesis of higher-order local *k*-harmonics or on image-domain reconstruction procedures; these procedures parallel concepts underlying SMASH and SENSE, respectively, yet it is conceivable that additional approaches can also be devised. A final point worth mentioning is the method's compatibility with all other improvements that have hitherto been developed for SPEN-like sequences, as demonstrated with the incorporation of multiband, SIR, or stimulated-echo approaches (see Supporting Information). A similar opportunity arises with regard to improving the resolution of other variants like bi-SPEN or xSPEN (40), as will be discussed in upcoming studies.

ACKNOWLEDGMENTS

We are grateful to Dr. Sagit Shushan (Wolfson Medical Center) and the Weizmann MRI team (Edna Furman-Haran, Fanny Attar and Nachum Stern) for their assistance in the human scans.

REFERENCES

1. Shrot Y, Frydman L. Spatially encoded NMR and the acquisition of 2D magnetic resonance images within a single scan. J Magn Resonance 2005;172:179–190.
2. Chamberlain R, Park JY, Corum C, Yacoub E, Ugurbil K, Jack CR, Garwood M. RASER: a new ultrafast magnetic resonance imaging method. Magn Reson Med 2007;58:794–799.
3. Nguyen T, Goerke U, Moeller S, Ugurbil K, Garwood M. Parallel imaging with RASER using multiband frequency-modulated excitation pulses. In Proceedings of the 17th Annual Meeting of the ISMRM, Honolulu, HI, USA, 2009.
4. Ben-Eliezer N, Irani M, Frydman L. Super-resolved spatially encoded single-scan 2D MRI. Magn Reson Med 2010;63:1594–1600.
5. Tal A, Frydman L. Single-scan multidimensional magnetic resonance. Prog Nucl Magn Reson Spectrosc 2010;57:241–292.
6. Goerke U, Garwood M, Ugurbil K. Functional magnetic resonance imaging using RASER. NeuroImage 2011;54:350–360.
7. Cai C, Dong J, Cai S, Li J, Chen Y, Bao L, Chen Z. An efficient deconvolution reconstruction method for spatiotemporal-encoding single-scan 2D MRI. J Magn Reson 2013;228:136–147.

8. Chen L, Bao L, Li J, Cai S, Cai C, Chen Z. An aliasing artifacts reducing approach with random undersampling for spatiotemporally encoded single-shot MRI. J Magn Reson 2013;237:115–124.
9. Chen Y, Li J, Qu X, Chen L, Cai C, Cai S, Zhong J, Chen Z. Partial Fourier transform reconstruction for single-shot MRI with linear frequency-swept excitation. Magn Reson Med 2013;69:1326–1336.
10. Chen L, Li J, Zhang M, Cai S, Zhang T, Cai C, Chen Z. Super-resolved enhancing and edge deghosting (SEED) for spatiotemporally encoded single-shot MRI. Med Image Anal 2015;23:1–14.
11. Li J, Chen L, Cai S, Cai C, Zhong J, Chen Z. Imaging with reference-less distortion correction and flexible regions of interest using single-shot biaxial spatiotemporally encoded MRI. NeuroImage 2015;105: 93–111.
12. Bohlen J, Bodenhausen G. Experimental aspects of chirp NMR spectroscopy. J Magn Reson A 1993;102:293–301.
13. Pipe JG. Analysis of localized quadratic encoding and reconstruction. Magn Reson Med 1996;36:137–146.
14. Garwood M, DelaBarre L. The return of the frequency sweep: designing adiabatic pulses for contemporary NMR. J Magn Reson 2001;153: 155–177.
15. Frydman L, Lupulescu A, Scherf T. Principles and features of single-scan two-dimensional NMR spectroscopy. J Am Chem Soc 2003;125: 9204–9217.
16. Frydman L, Scherf T, Lupulescu A. The acquisition of multidimensional NMR spectra within a single scan. Proc Natl Acad Sci 2002;99: 15858–15862.
17. Mishkovsky M, Frydman L. Principles and progress in ultrafast multidimensional nuclear magnetic resonance. Ann Rev Phys Chem 2009;60:429–448.
18. Goerke U. Spatial specificity in spatiotemporal encoding and Fourier imaging. Magn Reson Imaging 2016;34:562–573.
19. Ben-Eliezer N, Shrot Y, Frydman L. High-definition, single-scan 2D MRI in inhomogeneous fields using spatial encoding methods. Magn Reson Imaging 2010;28:77–86.
20. Schmidt R, Frydman L. New spatiotemporal approaches for fully refocused, multislice ultrafast 2D MRI. Magn Reson Med 2014;71: 711–722.
21. Bohlen J-M, Rey M, Bodenhausen G. Refocusing with chirped pulses for broadband excitation without phase dispersion. J Magn Reson (1969) 1989;84:191–197.
22. Leftin A, Rosenberg JT, Solomon E, Calixto Bejarano F, Grant SC, Frydman L. Ultrafast in vivo diffusion imaging of stroke at 21.1 T by spatiotemporal encoding. Magn Reson Med 2015;73:1483–1489.
23. Seginer A, Schmidt R, Leftin A, Solomon E, Frydman L. Reference-less reconstruction of spatiotemporally encoded imaging data: principles and applications to real-time MRI. Magn Reson Med 2014;72: 1687–1695.
24. Solomon E, Avni R, Hadas R, Raz T, Garbow JR, Bendel P, Frydman L, Neeman M. Major mouse placental compartments revealed by diffusion-weighted MRI, contrast-enhanced MRI, and fluorescence imaging. Proc Natl Acad Sci 2014;111:10353–10358.
25. Solomon E, Nissan N, Furman-Haran E, Seginer A, Shapiro-Feinberg M, Degani H, Frydman L. Overcoming limitations in diffusion-weighted MRI of breast by spatio-temporal encoding. Magn Reson Med 2015;73:2163–2173.
26. Solomon E, Shemesh N, Frydman L. Diffusion weighted MRI by spatiotemporal encoding: analytical description and in vivo validations. J Magn Reson 2013;232:76–86.
27. Liberman G, Frydman L. Reducing SAR requirements in multi-slice volumetric single-shot spatiotemporal MRI by two-dimensional RF pulses. Magn Reson Med 2016;77:1959–1965.
28. Schmidt R, Seginer A, Frydman L. Interleaved multishot imaging by spatiotemporal encoding: A fast, self-referenced method for high-definition diffusion and functional MRI. Magn Reson Med 2016;75: 1935–1948.
29. Pruessmann KP, Weiger M, Scheidegger MB, Boesiger P. SENSE: sensitivity encoding for fast MRI. Magn Reson Med 1999;42:952–962.
30. Sodickson DK, Manning WJ. Simultaneous acquisition of spatial harmonics (SMASH): fast imaging with radiofrequency coil arrays. Magn Reson Med 1997;38:591–603.
31. Blaimer M, Breuer F, Mueller M, Heidemann RM, Griswold MA, Jakob PM. SMASH, SENSE, PILS, GRAPPA: how to choose the optimal method. Top Magn Reson Imaging 2004;15:223–236.
32. Griswold MA, Jakob PM, Heidemann RM, Nittka M, Jellus V, Wang J, Kiefer B, Haase A. Generalized autocalibrating partially parallel acquisitions (GRAPPA). Magn Reson Med 2002;47:1202–1210.
33. Schmidt R, Baishya B, Ben-Eliezer N, Seginer A, Frydman L. Super-resolved parallel MRI by spatiotemporal encoding. Magn Reson Imaging 2014;32:60–70.
34. Uecker M, Lai P, Murphy MJ, Virtue P, Elad M, Pauly JM, Vasanawala SS, Lustig M. ESPIRiT—an eigenvalue approach to autocalibrating parallel MRI: where SENSE meets GRAPPA. Magn Reson Med 2014;71:990–1001.
35. Lustig M, Donoho D, Pauly JM. Sparse MRI: the application of compressed sensing for rapid MR imaging. Magn Reson Med 2007;58: 1182–1195.
36. Zhang T, Chen L, Huang J, Li J, Cai S, Cai C, Chen Z. Ultrafast multi-slice spatiotemporally encoded MRI with slice-selective dimension segmented. J Magn Reson 2016;269:138–145.
37. Feinberg DA, Setsompop K. Ultra-fast MRI of the human brain with simultaneous multi-slice imaging. J Magn Reson 2013;229:90–100.
38. Feinberg DA, Reese TG, Wedeen VJ. Simultaneous echo refocusing in EPI. Magn Reson Med 2002;48:1–5.
39. Reese T, Heid O, Weisskoff R, Wedeen V. Reduction of eddy-current-induced distortion in diffusion MRI using a twice-refocused spin echo. Magn Reson Med 2003;49:177–182.
40. Zhang Z, Seginer A, Frydman L. Single-scan MRI with exceptional resilience to field heterogeneities. Magn Reson Med 2017;77:623–634.

SUPPORTING INFORMATION

Additional Supporting Information may be found in the online version of this article.

Fig. S1. a: Extending the coverage afforded by SUSPENSE by means of multiband excitation along the slab-selective axis (two bands), plus SIR-based slice deconvolution (colored pulses within each band and colored FIDs; detailed processing not shown) within sensor-resolved multiband slabs. The sequence shows an optional stimulated echo block enabling an even higher multislicing without SAR penalties (3), which was not used in this example. **b**: Two-dimensional SPEN images following separation of the two slice-selective echoes along G_{RO} and FT along this axis, showing the multiband overlap. **b**: SENSE-based separation of the multibands, leading after SR to images with $1 \times 2 \times 2$ mm resolution and to the (x, y) coil sensitivity maps. **c**: SUSPENSE processing of the same data using a second-order spherical harmonic, leading to $1 \times 1 \times 2$ mm resolutions. Lower insets show identical slices (**b, c**), zoomed to highlight the finer delineation evidenced by the gray matter sulci (contoured in red). Additional acquisition parameters included the acquisition of 16 slices from a $20 \times 8.4 \times 2.6$ cm FOV in 6 s, using $G_e = 0.13$ G/cm, $T_e = 43.7$ ms, and $M_{spen} = 42$.

Fig. S2. Extending the coverage afforded by SUSPENSE by combining, along the slice-selective axis, a two-band excitation with the acquisition of six stimulated echo images arising from each encoded slab (7,20). Whole-brain coverage with 48 slices (4 slabs $\times$ 2 bands $\times$ 6 stimulated echoes/slab) was thus achieved in TR = 3 s. Images were processed with SUSPENSE and R = 5, leading to $1 \times 0.9 \times 2.5$ mm resolutions over a $20 \times 18 \times 12$ cm FOV. Green rectangles exemplify data that were simultaneously encoded in two bands. The images within each rectangle arise from different stimulated echoes (i.e., to sequentially excited slices encoded within the same slab).